Article

Digital Elevation Model Differencing and Error Estimation from Multiple Sources: A Case Study from the Meiyuan Shan Landslide in Taiwan

Yu-Chung Hsieh [1,2], Yu-Chang Chan [3,*] and Jyr-Ching Hu [2]

1   Central Geological Survey, MOEA, Taipei 235, Taiwan; hsiehyc@moeacgs.gov.tw
2   Department of Geosciences, National Taiwan University, Taipei 106, Taiwan; jchu@ntu.edu.tw
3   Institute of Earth Sciences, Academia Sinica, Taipei 115, Taiwan
*   Correspondence: yuchang@earth.sinica.edu.tw; Tel.: +886-227839910 (ext. 411)

Abstract: In this study, six different periods of digital terrain model (DTM) data obtained from various flight vehicles by using the techniques of aerial photogrammetry, airborne LiDAR (ALS), and unmanned aerial vehicles (UAV) were adopted to discuss the errors and applications of these techniques. Error estimation provides critical information for DTM data users. This study conducted error estimation from the perspective of general users for mountain/forest areas with poor traffic accessibility using limited information, including error reports obtained from the data generation process and comparison errors of terrain elevations. Our results suggested that the precision of the DTM data generated in this work using different aircrafts and generation techniques is suitable for landslide analysis. Especially in mountainous and densely vegetated areas, data generated by ALS can be used as a benchmark to solve the problem of insufficient control points. Based on DEM differencing of multiple periods, this study suggests that sediment delivery rate decreased each year and was affected by heavy rainfall during each period for the Meiyuan Shan landslide area. Multi-period aerial photogrammetry and ALS can be effectively applied after the landslide disaster for monitoring the terrain changes of the downstream river channel and their potential impacts.

Keywords: Airborne LiDAR (ALS); unmanned aerial vehicles (UAV); photogrammetry; digital elevation model (DEM) differencing; swath profile

1. Introduction

Multi-source, multi-period DTM data are not only a critical tool for research on the mechanism of landslides, but also considered as greatly useful information regarding active faults, earthquake disasters [1–4], and flooding/river bank erosion [5]. When it comes to the comparison of this type of terrain information, error estimation of data obtained in various periods using various techniques becomes crucial. Almost every technology, including theodolites, GPS, photogrammetry, InSAR, airborne LiDAR (ALS), and ground LiDAR, has its application ranges and restrictions in terms of spatial and time scales when employed to obtain 3-D terrain data [6,7]. By comparing the information with various precision and resolution methods that are collected during different periods, these multi-method, multi-period data of digital terrain models (DTM) have been used in landslide mechanism-related research [8], observations of surficial activity [9–11], landslide volume calculations [12–14], and volume variation estimations [15], as well as disaster scale assessment and simulation [16].

Most of the previous comparative studies on multi-period DTM data have adopted ground control points, e.g., the discussion of landslide and river terrain variation by comparing the DTM data from ground measurements and those from aerial photogrammetry and ALS measurements [10,17–19], analysis of river terrain variation and slope earthflows by contrasting between two-period [20,21] or three-period [22] ALS data and ground measurement data, evaluation of earthflow terrain variation using airborne and ground LiDAR data, and error assessment of these two techniques [23], using InSAR-derived DTM to discuss terrain changes before and after the landslide event [7], and error assessment based on the two LiDAR datasets of Taiwan [24]. All of these studies mentioned above were conducted based on accessible ground measurement points. However, difficulties associated with ground measurements might occur if the target areas were located on high and steep mountains or densely vegetated areas, which could potentially affect the assessment of errors. Moreover, Tseng *et al.* calculated errors based on the undisturbed areas [25] and regarded the standard deviation of distribution of elevation difference as the average difference and error range of the two-period digital elevation model (DEM), respectively. Such an assessment method tended to be affected by the selected undisturbed areas. Hence, data obtained using different DTM generating techniques under various terrains or landscapes could lead to varied errors, which would eventually impact the rationality of the subsequent analysis or assessment.

Due to the highly unpredictable feature of landslide incidents, few practically measured landslide volume values exist. Most research work conducted in the past evaluated slide volume by measuring the landslide area on the obtained image and then estimating the average depth [26–28]. However, the certainty of landslide depth is often difficult to evaluate due to the lack of terrain information before the disaster, which would affect the accuracy of landslide volume estimation. As a result, there also exist a number of studies where statistical/empirical equations, *i.e.*, relations between area and volume derived by compiling a large quantity of landslide cases, are used to approximate the potential landslide volume based on a certain landslide area. Nevertheless, this type of method is also restricted by various factors such as area features, landslide type, slope morphology, and rock properties [29]. With the development of DTM data, it has become feasible to adopt various techniques such as photogrammetry, ALS, and ground LiDAR, along with multi-period terrain information to calculate landslide volume [10,12–16,19]. This work used the multi-period aerial photogrammetry, UAV, and ALS techniques to explore the application of data generated from different techniques in DEM differencing analysis after landslide hazards, as well as to calculate the earthflow volume produced by massive landslides. Specifically, through error assessment of multi-source, multi-period DTM data obtained from a densely-vegetated mountain area, this research attempted to examine the applicability of various techniques in massive landslides under such terrain conditions. The landslide volume and the subsequent volume variation were also calculated using DTM data from multiple periods. This research enables researchers who apply multi-period DEMs to know more about the characters, activities, and potential effects of landslides and, thereby, offering effective guidance on the assessment of landslide hazards.

2. Materials and Methods

2.1. Study Area

In 2008, Taiwan region was struck by the massive rainfall brought by Typhoon Sinlaku. The mountainous area in Central Taiwan received over 1000 mm of rainfall, with a maximum accumulated precipitation of more than 1600 mm [29], which caused severe geological hazards in this area. The restaurant buildings in the Lushan hot spring area in Nantou County collapsed and the Houfeng Bridge in Taichung City was damaged by floods [30]. The Meiyuan Shan landslides (Figure 1) occurred near Ren'ai Township, in Nantou County in Central Taiwan, near Huisun Experimental Forest Station, within the river basin of Meitangan River of the Beigang River system. The significantly heavy rain brought by Typhoon Sinlaku on 14–15 September 2008 caused the rain gauge at the Qingliu station

to reach 761 mm. As a result, a large-scale landslide with an area of about 0.9 km² occurred on the southeastern slope of Meiyuan Shan (1785 m), which led to a large landslide. Subsequently, the large body of rocks and sediments propagated downstream with water, depositing at the confluence of the Beigang and Meitangan Rivers (Figure 2). The base of the Tou 80 County Road and the slope next to the camping area within the Huisun Experimental Forest Station were seriously hollowed out, and the collapsed sediments congested the Meitangan River, forming a landslide dam. The main geomorphological features of this area (marked by the blue boundary in Figure 1) are described here:

- Ridges stretch from Baxianshan in the northeast to Meiyuan shan in the southwest, with the dominant southeast slope aspect;
- The flow of the Meitangan River system is naturally bounded by the ridge boundaries, *i.e.*, flowing from the northeast toward the southwest and then converging into the major river in this area, the Beigang River;
- In addition to the Huisun Experimental Forest Station, villages such as Qingliu, Chungyuan, and Meiyuan are all located along the bank of the Beigang River.
- While these villages can communicate with the outside area through the county road, the study area cannot be reached through any roads other than walking in the countercurrent direction.

Near the study area, there is a rain gauge station close to Qingliu Village set by the Central Weather Bureau and a flowmeter set by the Water Resource Agency, Ministry of Economic Affairs can also be found downstream (Figure 1). The data from the rain gauge station and the flow monitoring station during 2005 to 2013 are shown in Figure 3.
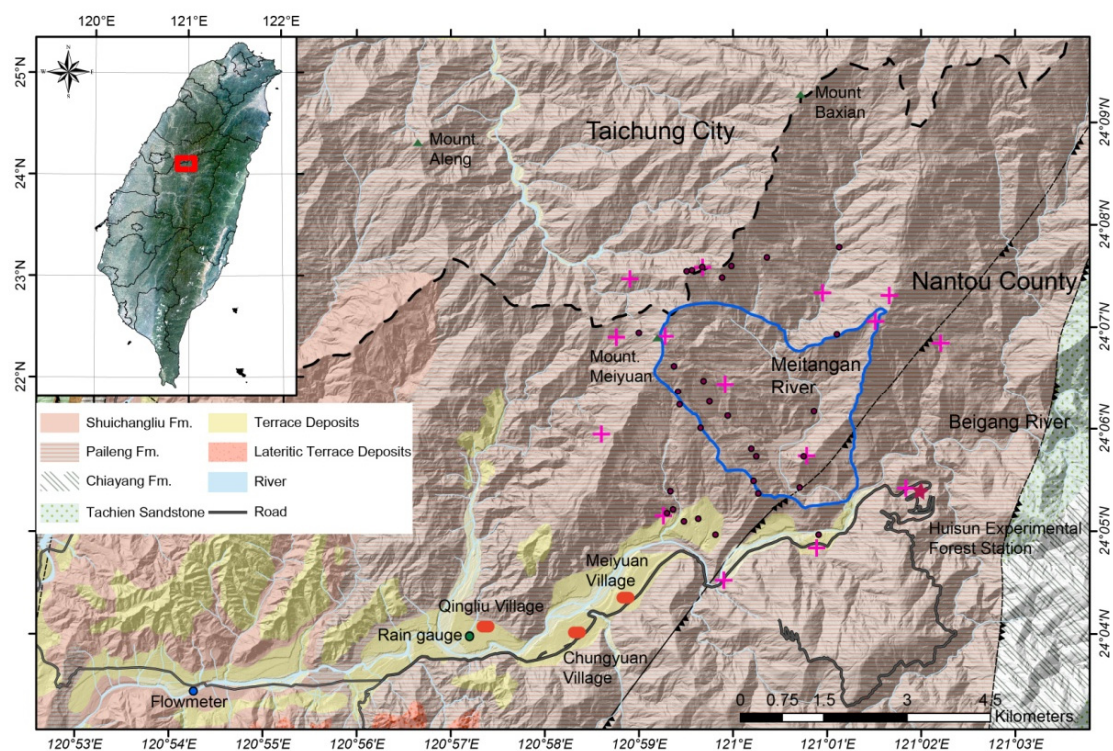

Figure 1. Geological map and geographical position of the study area. The blue line shows the range of orthoimage and digital terrain model (DTM) data generated in this research. There is a rain gauge (green point) and a flowmeter (blue point) in the adjacent area. Multiple residential villages are located downstream of the study area. The study area is shown in red square within the upper-left index map. Three data sets derived from aerial photogrammetry in this research used the same 15 ground control points shown as pink cross marks. The UAV dataset used the 30 ground control points shown as dark brown dots.
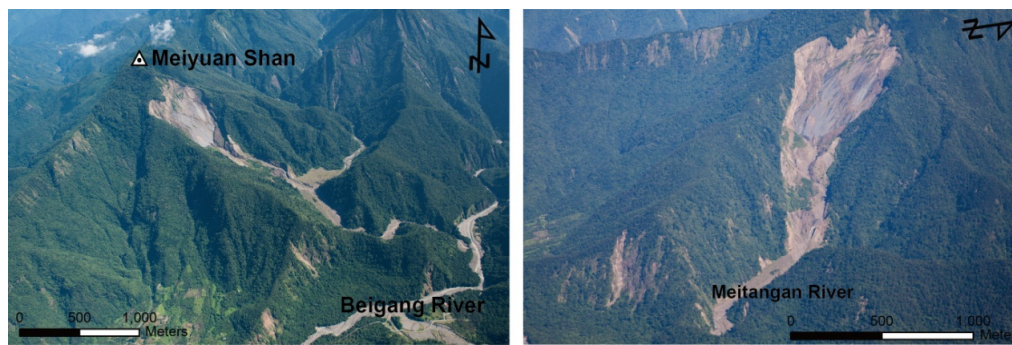
Figure 2. Panorama of the Meiyuan Shan landslide. The left image, a view from the south of Meiyuan shan, illustrates that the Meiyuan shan terrain along the northeast–southwest direction is a dip slope. It also shows the alluvial fan generated by rock slides and debris flows. The Meitangan River feeds into the Beigang River, the main river in this area, which is shown at the right side of this image. The right image, a view from the east of the Meiyuan Shan landslide, displays the relatively smooth surface of the zone of depletion revealed after the landslide. A large body of rock and sediments can still be clearly observed at the foot of the slope.
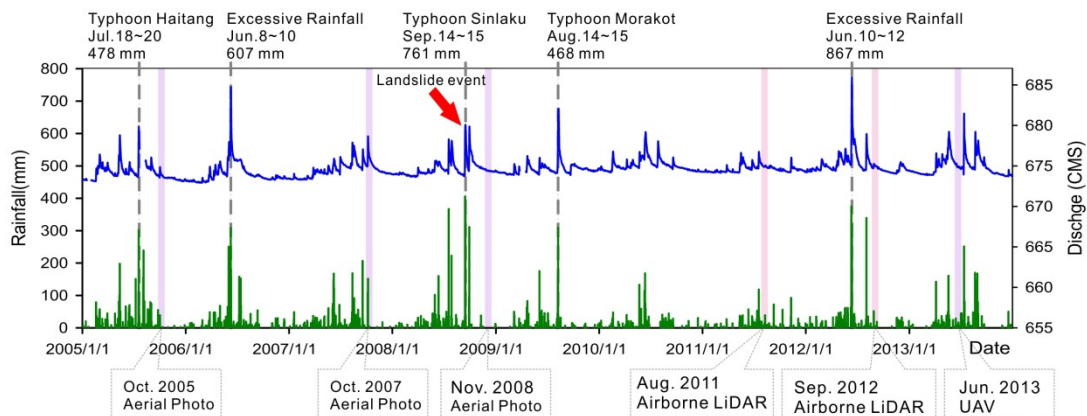

Figure 3. The green bars show the rainfall data recorded by the Qingliu rainfall monitoring station from 2005 to 2013. The blue lines are the flowrate data measured in Beigang River, and the dash lines representing typhoon and torrential rain incidents during this period of time. The purple lines indicate the times when aerial photography and ALS measurements were conducted in this study.

2.2. Geological Setting

This area is part of the Hsueshan Range zone in terms of geological setting. The exposure strata of its adjacent areas contain the Tachien Sandstone, Chiayang Formation, Paileng Formation, Shuichangliu Formation, terrace deposits, and lateritic terrace deposits (Figure 1). The study area was mainly in the range of the Paileng Formation, with exposure rocks of white or grey, fine or coarse quartzitic sandstone, and interbedding of grey dense sandstone and dark grey argillite or slate. With high rock strength and weather resistance, this type of sandstone is a major feature of the main northeast–southwest ridge in this area, forming the above-mentioned dip slope terrain. The main geological structures in this area are the Meiyuan Fault and the Guandaosan Fault. The Meiyuan Fault stretches from northeast to southwest, coincidently passing through the confluence of the Yangan River and the Beigang River within the study area. It is an eastwardly tilted, high-angle thrust fault, located west of the study area. The Guandaosan Fault lays southeast of the Meiyuan Fault, running almost south to north. It is also an eastwardly tilted, high-angle thrust fault, with the Paileng Formation to its west and the Tachien Sandstone and slate of Chiayang Formation to its east.

2.3. Aerial Photogrammetry

Aerial photogrammetry is one of the commonly adopted techniques for obtaining 3-D terrain information, which can be used to generate DTM data from aerial images through digital photogrammetry. It is often employed in studies of landslide geomorphology. In most cases, complete DTM data prior to the landslide event are not necessarily available. In a situation like this, however, historical aerial images can be used to generate DTM through digital aerial photogrammetry. The Aerial Survey Office, Forest Bureau (ASO), has conducted aerial photography for Taiwan forests on a regular basis, the images obtained from which could be used as orthoimage and DTM data before landslide events for analysis. Each photo had to be checked for factors, such as cloud content and the existence of fog to ensure the image quality for subsequent processing. Photos would not be usable with blurry images, fog, excessive shadows, or clouds (shadows). By searching the historical images taken before the 2008 Meiyuan Shan landslide incident, three periods of datasets are suitable for post-processing, *i.e.*, those taken on 22 October 2005, 23 October 2007, 11 November 2007, 10 October 2008, and 30 November 2008 were selected and obtained from Geoforce Company and the ASO historical aerial photogrammetry database [31]. The set from 2005 contained 203 images taken by ULTRACAM. The set from 2007 was composed of four images taken by RMK TOP and seven taken by an Intergraph digital mapping camera (DMC). The set from 2008 had seven images taken by DMC and an air route covered by a Leica airborne digital sensor 40 (ADS40). Ground sample distances (GSD) were 0.17 m, 0.19 m, and 0.18 m, respectively. All three datasets used the same 15 ground control points and were processed by SimActive software and aerial photogrammetry work stations. The processing of the aerial photogrammetry data is briefly described here:

- After appropriate aerial images were chosen and aerotriangulation mapping was done, models based on the accurate parameters of exterior orientation of every image and superimposition of high-precision GPS coordinates were made.
- When conducting aerotriangulation adjustment, the 15 ground control points were also taken into consideration to improve the accuracy of the parameters of exterior orientation. The control point errors of three data sets after aerotriangulation adjustment are shown in Table 1. The distribution of the 15 ground control points are shown in Figure 1.
- Then stereo image pairs, DTM, as well as orthoimages, could eventually be generated. The resolutions of orthoimages and DTM were 25 cm and 2 m, respectively.

Table 1. The control point errors of three datasets after aerotriangulation adjustment.

	Maximum Changes (m) at Control Points			RMS of Changes (m) at Control Points		
	X	Y	Z	X	Y	Z
2005	0.4045	0.3814	−0.3926	0.2087	0.2043	0.1563
2007	0.0636	0.1395	−1.1654	0.0315	0.0519	0.3373
2008	−0.0355	0.0437	−0.0197	0.0230	0.0260	0.0108

Unmanned aerial vehicles (UAV) have been applied more and more widely in national defense, military affairs, and civil applications in recent years. It has also become one of the main DEM techniques due to its advantages of low operation costs, high data processing speed, low flying height, and convenient flying preparation. UAVs are an important technique in post-disaster response when it comes to a confined environment, particular terrain, or the need for consistent monitoring after disasters. For the reasons mentioned above, this study also adopted UAV techniques to survey the Meiyuan Shan landslide area in June 2013, using a fixed wing drone with a flying height of 2500–2750 m, a Canon 500D camera with a lens with focal length of 50 mm, and planned ground sample distance (GSD) of 8–19 cm. During the flight operation, 868 images were taken, which were then processed using the same method applied for aerial photogrammetry data with the Pix4D software. Thirty

ground control points shown in Figure 1 were used for UAV aerial photogrammetry. The RMS of changes at control points were 0.055 m (x), 0.018 m (y), and 0.362 m (z). Resolutions of the generated orthoimage and DTM were 25 cm and 2 m, respectively.

2.4. Airborne LiDAR (ALS)

For regional wide-range topographic surveying and mapping, ALS is currently considered as the technique able to obtain terrain data with the best resolution and precision. The data used in this study were measured by the Geological Survey in August 2011 and September 2012, respectively. The former was a surveying and mapping program for DTM data over the whole island of Taiwan conducted by the Geological Survey. The program was aimed to obtain DTM data with a resolution of 1 m; that is, a point cloud with a density of 1.5 points/m^2 was expected at a monitoring height of 800 m. Flight parameters are shown in Table 2. The latter was the repeated LiDAR DTM survey work for the Meiyuan Shan landslide, data which were assumed to be the same as the former. Flight parameters of this program are also shown in Table 2. These two ALS datasets were processed using the same method, as given here:

- Data obtained from the flight operation were calculated to get information about each air route for flight strip adjustment.
- Original point clouds were gained after adjustment, followed by point cloud classification.
- The point clouds of these two operations were divided into four categories: ground points, non-ground points, water body points, and outlier point clouds.
- Then the digital surface model (DSM) and digital elevation model (DEM) were generated. The DSM represents the Earth's surface, including all objects on it. The DEM represents bare ground surface without any objects, like vegetation and buildings. The term DTM comprises both DSM and DEM in this study. The two LiDAR survey programs took aerial photos, which were used to generate orthoimages with a resolution of 25 cm. This study adopted data from both 2011 and 2012. LiDAR data of 2011 were set as the benchmark for precision assessment due to wide coverage and completeness.

For comparison purposes, the TWD 97 ground coordinate system [32] was employed for all of the data sets, and the Taiwan Vertical Datum 2001 (TWVD 2001) [33] was selected as the vertical coordinate system.

Table 2. Flight parameters and scanning system settings.

	2011	2012
Date	2011/8	2012/9
Sensor system	Leica ALS60	Riegl/LMS-Q680i
Flying height (m)	2700	3000
Flying speed (kts) [1]	100	100
Pulse frequency (KHz)	53.4	150
Field of view (FOV) (°)	40	40
Scanning swath width (m)	1175	1223
Strips overlapping (%)	52	50
Laser pulse density (pt/m^2)	1.8	2. 2
Resolution (m)	1.0	1.0

[1] 1 kts = 1.852 km/h.

3. Results

3.1. Orthoimage

This study employed orthoimages generated using various aerial photogrammetry cameras from six different periods, and the results are shown in Figure 4. These aerial photogrammetry orthoimages

show changes before and after the Meiyuan Shan landslide. Figure 4a,b, obtained prior to the disaster, show that only occasional shallow landslides occurred on some upstream slopes. Figure 4c–f were obtained after the disaster. It can be clearly seen that, in 2008, a landslide dam was formed due to a large body of landslide rocks, and a blue waterbody existed in the river channel at the toe of the landslide. Parts of the waterbody are still visible in Figure 4d, and the area of the landslide dam has reduced to less than half, though still existing in this basin. By comparing Figures 3 and 4 it can be inferred that the landslide dam might have existed for almost four years before being damaged by the torrential rain in June 2012.
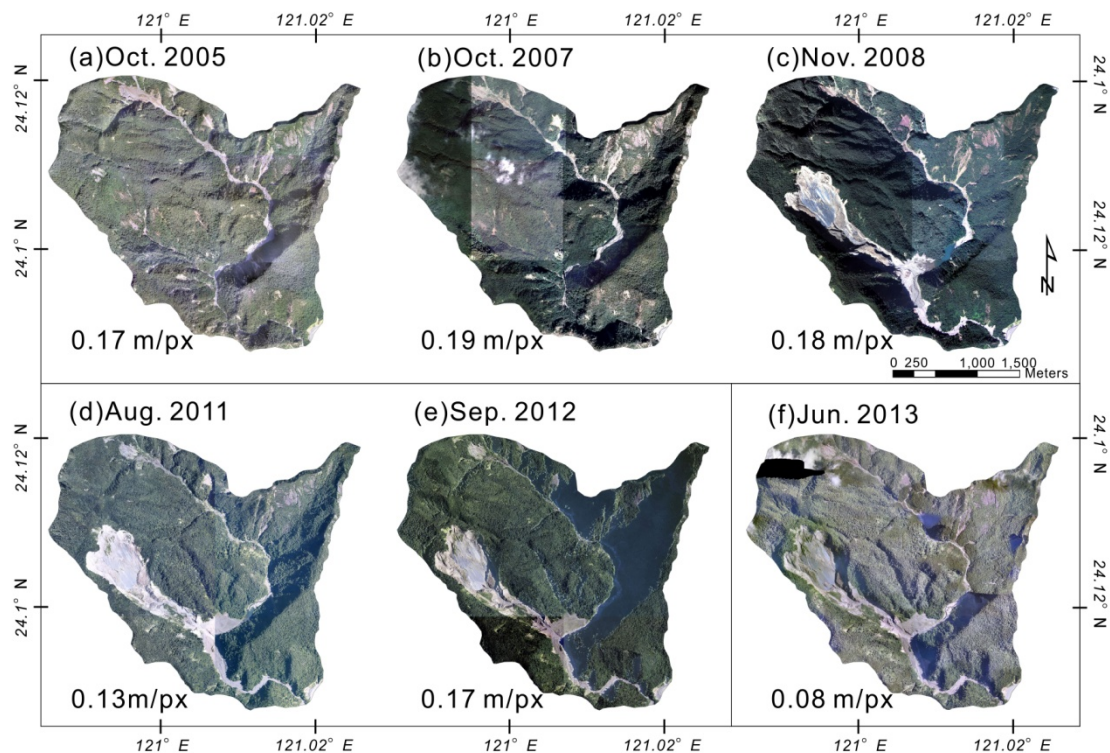

Figure 4. Orthoimages generated using various aerial photogrammetry cameras from six periods. (**a**–**c**) historical aerial photogrammetry images; (**d**,**e**) taken under the ALS survey task; and (**f**) a photograph by an unmanned aerial vehicle (UAV).The number is ground sample distance (GSD). The large-scale landslide area in (**c**–**f**) is the Meiyuan Shan landslide area, in which specific landslide characteristics can be observed from top to middle and then to the foot of the slope. The blue waterbodies distributed in (**c**,**d**) are where the landslide dams are located.

3.2. Digital Terrain Model

This study used six periods of DTM data, which comprise both DEM and DSM data, obtained from aerial photogrammetry, ALS, and UAV techniques. All three DTM techniques can be used to generate DSM and DEM data. Since the actual ground points under plants can be scanned by the infrared laser, ALS is able to obtain the DEM data of actual ground elevation without being affected by ground vegetation [34,35]. However, aerial photogrammetry is only able to gain the actual ground elevations of exposed areas because of the limited ability of only mapping ground elevation displayed in the images. In plant-covered areas, potential real elevations can be determined from DSM data and elevations of the exposed areas, which might produce relatively large errors. In this study, the discussed landslide area and affected river channel were both considered as exposed areas without plant coverage. Hence, DSM data were used to analyze terrain change before and after the landslide disaster. Results of this comparison are shown in Figure 5.
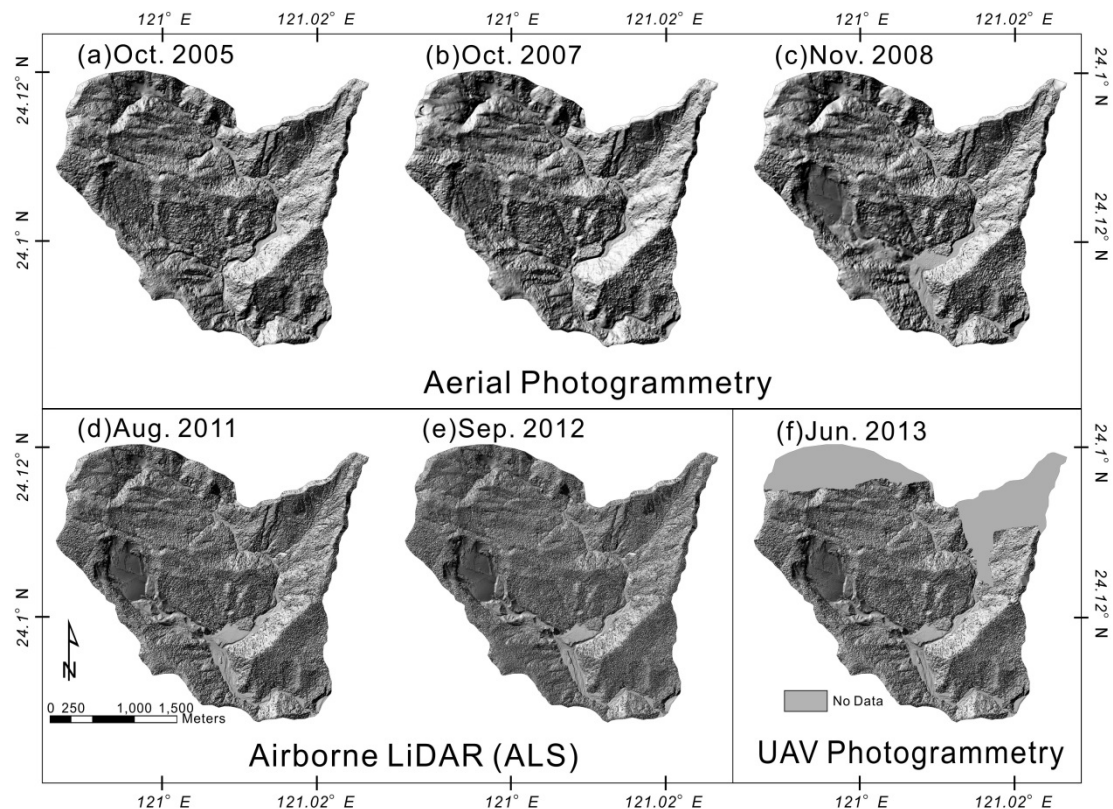
Figure 5. Digital Surface Model (DSM) images generated from six periods. (**a**–**c**) are the traditional aerial photogrammetry images; (**d**,**e**) were taken by the ALS technique; and (**f**) obtained through UAV aerial photogrammetry. The uniform grey areas shown in the images represent lack of information due to clouds.

3.3. Error Estimation

Error assessment is critical information for DTM data users. Most users do not necessarily participate in the production of DTM data. When it comes to comparative analysis of DTM data, especially for those areas with terrain variation, differences of data obtained from different levels of precision would affect the results of any comparison. Most of the previous comparative studies as aforementioned in the introduction on multi-period DTM data have adopted ground control points to evaluate errors of individual DTM data sets. From the perspective of general users, this study conducted error assessments for mountain and forest areas with poor traffic accessibility using limited information, including error reports obtained from the data generation process and comparison errors of terrain elevations.

Generally speaking, users can get aerotriangulation errors and interpolation errors from the data generation process. Aerotriangulation errors are the errors in X, Y, and Z directions after the aerotriangulation adjustment, which can be obtained using survey adjustment software and calculating the difference between aerotriangulation matching points and applied ground control points, *i.e.*, the aerotriangulation σ shown in Table 3. Interpolation errors refer to the errors originated during interpolation, which is used to generate gridded DTM data after stereo pairs are matched. This type of error can be obtained by calculating the difference between the estimated elevation of gridded data and the actual ground elevation, as interpolation σ shown in Table 3. These two errors then can be used to calculate the total error based on the simple error propagation theory, as shown in Equation (1) [36]. Among these periods, the gridded DTM data from 2011 and 2012 were generated based on point

clouds using the ALS technique. Therefore, their total errors were achieved directly from the difference between the actual terrain measured elevation and the calculated elevation:

$$\sigma_{\text{total}} = \sqrt{\sigma_1{}^2 + \sigma_2{}^2} \tag{1}$$

Ground control points or image characteristic points are usually assigned to those identifiable, flat, hardly-vegetated spots or characteristic points of buildings for error estimation. They can be used in terrain GPS measurements to represent the real ground elevation. However, most landslide disasters occur in areas with high mountains and forests that are rugged and hardly accessible. Hence, selection of the image characteristic points would be greatly restricted, and the representativeness of the error assessment would be affected due to the insufficiency of measurement points. The LiDAR data used in this study were from 2011 and 2012. In order to make error assessments for each period complete and representative, the 2011 DEM data were adopted as the terrain benchmark due to their wide coverage. The elevation values at selected characteristic points of each period were mapped with the elevation values at the same points of the 2011 DEM. Then their differences were the errors [37], as shown in Table 3. Errors in this paper were all given in the form of root-mean-square error (RMSE), which is a commonly used error expression [38,39]. The terrain change could be found by comparing data from different periods. Therefore, the errors between the two successive periods were also calculated using the described error relation. The results are shown in Table 4.

Table 3. Accuracy evaluation of datasets obtained from different periods.

	2005	2007	2008	2011	2012	2013
Aerotriangulation σ (m)	0.156	0.337	0.108			
Interpolation σ (m)	0.242	0.218	0.195			
σ_{total} (m)	0.288	0.402	0.223	0.150	0.170	0.247
$\sigma_{\text{2011 DEM}}$ (m)	0.750	0.510	0.430		0.180	0.580

Table 4. Accuracy evaluation of two terrain datasets obtained from two successive periods.

	2005–2007	2007–2008	2008–2011	2011–2012	2012–2013
σ_{total} (m)	0.494	0.459	0.269	0.227	0.300
$\sigma_{\text{2011 DEM}}$ (m)	0.907	0.667	0.455	0.234	0.607

3.4. DEM Differencing

The method of using multi-period DTM data to investigate terrain evolution has recently been applied in various studies regarding river bed sediment transport, landslide, and earthflow [16,25,40–42]. One of the most straightforward ways is to subtract an earlier terrain elevation from a later one. As six periods of DTM data were employed in this work, five values of terrain elevation change could be successively calculated in chronological order. Data from 2005–2007, as shown in Figure 6a, demonstrated the terrain change of this basin before the landslide disaster, whereas the other four periods, as shown in Figure 6b–e, demonstrated the terrain changes observed in each year after the disaster. Warm colors with negative values stand for a decrease in terrain elevation in these images, *i.e.*, the occurrence of surface erosion; and cold colors with positive values represent an increase in terrain elevation, *i.e.*, the occurrence of surface deposition. Through the color changes, the terrain evolution and sediment transportation of the river channel prior and subsequent to the landslide incident can be observed directly.

Figure 6a mainly shows sediment deposition in the river channel from the upstream catchment before the landslide. Figure 6b demonstrates the terrain change before and after the incident, in which the zone of depletion of the Meiyuan Shan landslide (shown in yellow and red) is the main source of sediment and the blue area is the zone of sliding sediment deposition. Obviously in the blue area,

a large body of sediments deposited from the middle of the slope all the way to the foot, creating a river blocking at the foot of the slope, which is typical for landslide terrain. Figure 6c–e illustrate sediment erosion and deposition in different areas within the landslide affected range after the incident. There was small-scale erosion in the zone of depletion after the incident, but the majority of the area did not change. Erosion was the main feature in the zone of sediment deposition, which was the main source of the sediments downstream after the disaster. Regarding the river channel range evolution after the incident, deposition, and partial erosion has happened since the disaster until the year of 2011 and elevation only changed by several meters; whereas, river channel erosion played a critical role from 2011 to 2013, and elevation changes due to river bank erosion were be more than 10 m in some parts. As for the unchanged areas, it is difficult to homogenize the DTMs from different time periods because in these areas vegetation was dominant. The DTMs from these areas tended to show differencing noises that were either resulted from tree growth, wind effects, or forest farming. For this reason, we have intentionally avoided the unchanged areas and masked them out before our landslide change analysis. As for the landslide affected areas, they are generally bare grounds and the DTMs from these areas show much better quality in comparison with those from the unchanged areas. Thus, we mainly focused on the landslide and river channel areas where vegetation was limited.
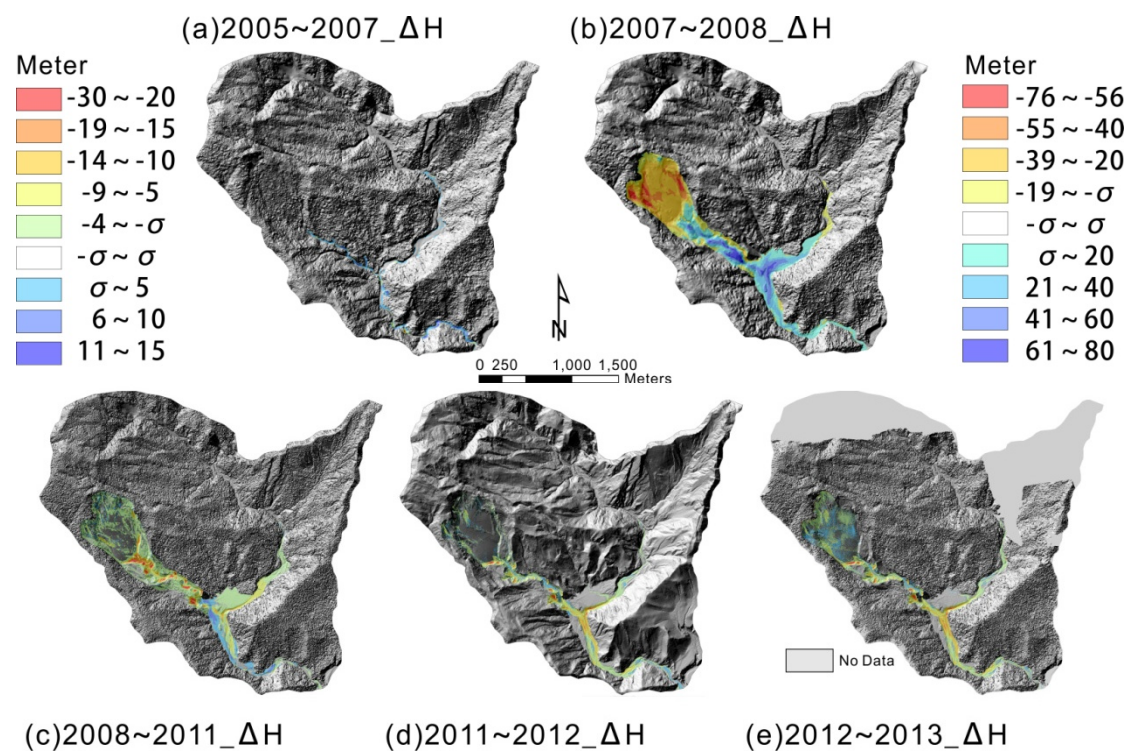

Figure 6. Images of terrain change over five periods calculated from multi-period digital terrain model (DTM) data in the Meiyuan Shan area. The color scale illustrates values of terrain change, where warm colors stand for an elevation decrease due to erosion, and cold colors represent an elevation increase led by the effects of deposition. (**a**) Terrain change (October 2005~October 2007) before the September 2008 landslide event; (**b**) Terrain change (October 2007~November 2008) right after the September 2008 landslide event. Please notice the markedly difference in elevation changes due to the fresh landslide event; (**c**) Terrain change (November 2008~August 2011); (**d**) Terrain change (August 2011~September 2012); (**e**) Terrain change (September 2012~June 2013). The scale for (**a**,**c**–**e**) is shown on the left; whereas, the one for (**b**) is shown on the right. σ is the total error of the two periods of DTM data shown in Table 4.

3.5. Volume Estimation

Volume calculations were implemented in the Spatial Statistics module of ArcGIS, and a brief description is given here:

- Calculate the difference between the elevation values at a characteristic point from a later DTM dataset and an earlier dataset, which could be either positive or negative.
- If resolution discrepancy of DTM data exists between the two periods, the higher resolution scale should be converted to the lower one.
- Then the deposition volume (positive result) and erosion volume (negative result) can be calculated based on the same resolution level.
- The summation of these two values is the net rock volume change over this period.
- Furthermore, with the calculated deposition area and erosion area and the previously obtained error value, the volume estimation error can also be gained, as shown in Table 5 [15].

Volume change showed a positive value in 2005–2007, but it remained negative in the other four periods. This suggested that earth and rocks brought from upstream of this basin deposited in the area before the Meiyuan Shan landslide; on the other hand, the earthflow produced from the landslide became the main source of sediments in Beigang River after the disaster, as indicated by the negative sign. The volume loss reached its peak in the disaster year and has decreased every year since then. During 2007–2008, the erosion and deposition volumes were 16.7 and 12.6 million m^3, respectively. Neglecting rock volume expansion and supplemental debris from upstream, at least 16.7 million m^3 of sediment were moved during the Meiyuan Shan landslide.

Table 5. Volumes of erosion, deposition, and volume change within the Meiyuan Shan landslide area estimated using digital terrain model (DTM) data obtained from multiple periods.

Event		Area (m^2)	Volume (m^3)	Volume Change (m^3)
2005–2007	Erosion	27,768	35,800 $\pm$ 25,185	272,700 $\pm$ 139,939
	Deposition	126,520	308,500 $\pm$ 114,754	
2007–2008	Erosion	642,851	16,773,400 $\pm$ 428,782	$-$4,132,500 $\pm$ 788,122
	Deposition	539,641	12,640,900 $\pm$ 359,940	
2008–2011	Erosion	767,337	2,708,100 $\pm$ 349,738	$-$2,392,000 $\pm$ 432,115
	Deposition	182,367	316,100 $\pm$ 82,977	
2011–2012	Erosion	492,829	1,797,400 $\pm$ 115,322	$-$1,644,400 $\pm$ 218,042
	Deposition	438,973	153,000 $\pm$ 102,720	
2012–2013	Erosion	605,620	817,700 $\pm$ 407,284	$-$705,500 $\pm$ 534,870
	Deposition	150,562	112,200 $\pm$ 127,586	

3.6. Profiles

It is a common analytical method to discuss terrain evolution using terrain profiles. Most traditional methods generate terrain profiles by extracting elevation values passing through a straight line. However, pure line-extracting generated profiles often fail to truly represent the real terrain [43]. When generating profiles using a single straight line, the selection position is not likely to be objective, and it also might be subject to stochastic terrain or deviation. Thus, it is possible to generate misleading or incorrect information. In order to avoid or mitigate these stochastic deviations and their miscomprehension, more profile lines can be added. As a result, a profiling method that stack elevation values on parallel, equally-spaced tangents has been developed, *i.e.*, the swath profile method. Applications of the swath profile method can often be found in the analysis of large-scale regional terrain issues, such as tectonic structures or landslides [44–46].

To discuss terrain and river channel changes before and after the large-scale landslide incident, both conventional straight line profiling and swath profiling techniques were used in this study to generate profiles. For the conventional straight line profiling method, the starting and ending points were first selected, and elevation values between the points were calculated. A terrain profile could be eventually generated based on the distribution of elevations. The spacing between elevation values was set at the DEM resolution in this study. In addition to terrain profiles calculated using the straight line method (Figure 7), based on artificial selection, the profiling calculation was also conducted using polyline profiles over the critical range (Figure 7). For a swath profile, a rectangular area is usually selected as the target. Then DEM data within this rectangle are rotated so that the side to be profiled is parallel with the south to north direction. Then, the maxima, minima, average, and standard deviation of each elevation row can be calculated and drawn in profiles. The minima scenario was employed in this work to generate profiles (Figure 8). Additionally, irregular areas were also selected to generate swath profiles. Similarly, DEM data within this irregular area were rotated so that the side to be profiled was parallel with the south to north direction before generating profiles (Figure 8) using the above-mentioned calculation approach.
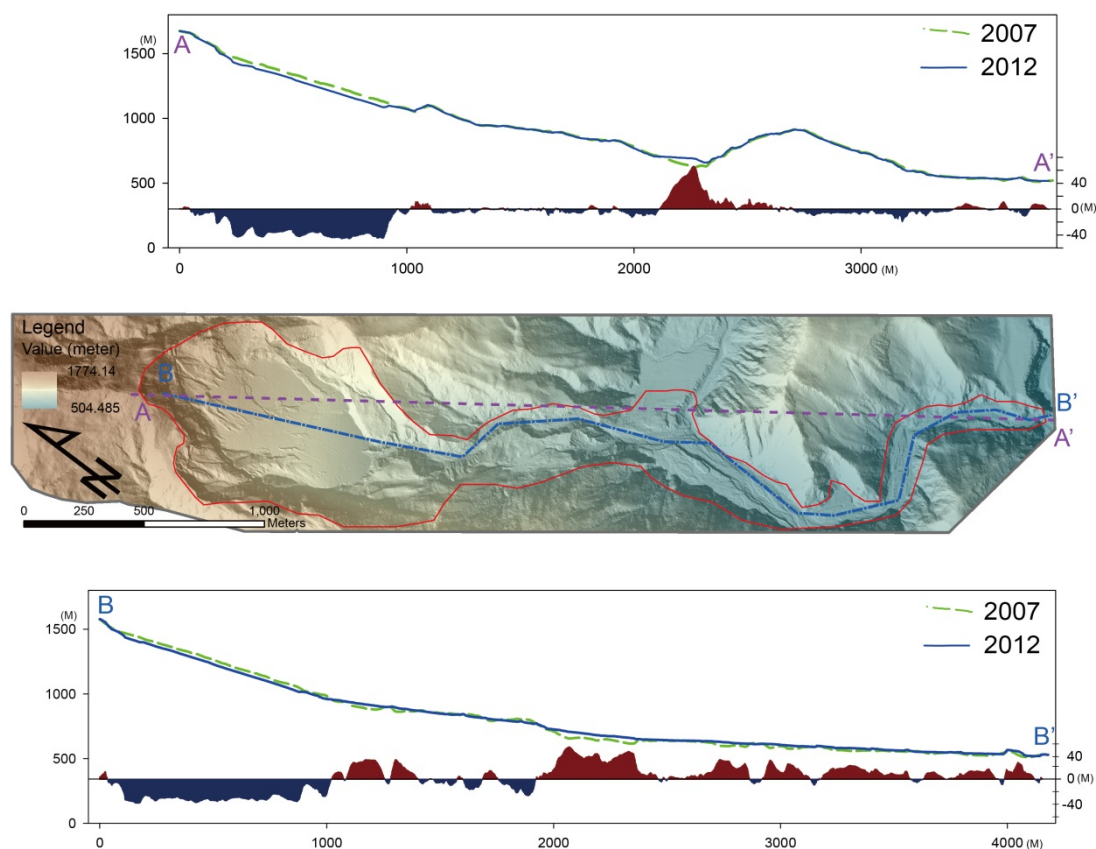

Figure 7. Straight line and polyline profiles based on terrain data obtained in 2007 (**before landslide**) and 2012 (**after landslide**). The purple A–A' dashed section shown in the middle represents the straight line profile, whose results are shown in the top; the blue B–B' section in the middle represents the polyline profile, whose results are shown in the bottom. The bottoms of the profile subfigures illustrate the elevation changes during 2007–2012, where dark blue denotes elevation decrease, while dark red denotes elevation increase.
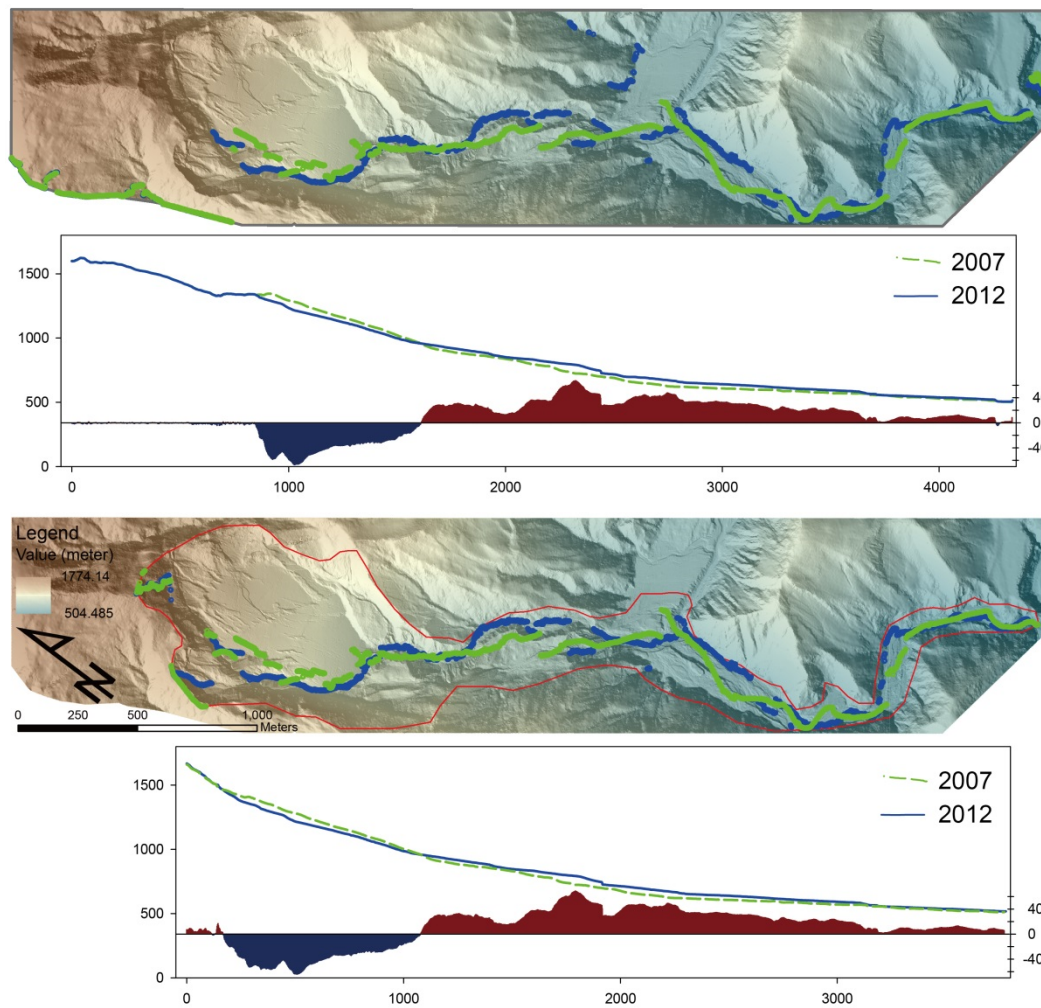
Figure 8. Swath profile calculation based on the terrain data obtained from 2007 (**before landslide**) and 2012 (**after landslide**). The first and the third subfigures show the swath profiles calculated using different target areas, *i.e.*, the entire rectangular range and the zone of depletion and the river channel, respectively. The results are, respectively, shown in the second and the fourth subfigures, where the green dashed line represents the elevation of 2007 while the blue line represents the elevation of 2012. The positions of sampling points are shown with the same colors in their corresponding maps. The bottoms of the profile subfigures illustrate the elevation changes during 2007–2012, where dark blue denotes elevation decrease, while dark red denotes elevation increase.

4. Discussion

4.1. Use of Data and Error Estimates

The six periods of DTM and orthoimage data used in this study were obtained from various aerial vehicles using multiple techniques such aerial photogrammetry and ALS. The generated data all had different errors that originated from their data generation methods and flight operations. Therefore, in a DTM application, the data acquisition procedure needs to be carefully determined once the data quality requirement is known. This is especially true for those flight parameters regarding the target area that would affect data resolution and errors, such as flying height, flying speed, flight direction, and overlapping strips. For terrain data produced using aerial photogrammetry, the elevation error is, generally speaking, about 0.2~1.3 m [37,38]. In a normal processing approach with sufficient ground control points, errors are mostly determined by the value of GSD [38]. Elevation error of ALS, on the other hand, is about 0.15~0.3 m [24,39,47]. Under regular processing, errors tend to be impacted by

slope angle, plant type, and vegetation density; though, generally, errors of bare flat areas would be superior to those of bare slope areas and errors of hardly vegetated areas would be superior to those of densely vegetated areas. For the six periods of DTM data generated in this work, with the difference between the elevation of set control points and calculated elevation, the statistical data errors were expressed in the form of RMSE. For the four periods of data generated using aerial photogrammetry, the errors of σ_{total} ranged from 0.22 m to 0.40 m (Table 3). The comparison with the image GSD values indicated that σ_{total} error was 0.98~2.1 times that of GSD, which was in good agreement with similar previous studies [37,38]. This suggested that the precision of generated DTM data in this work based on historical aerial images and UAV images using aerial photogrammetry was suitable for landslide analysis.

The method of estimating errors via ground control points could provide reference for applications. However, due to the facts that most landslide areas are often located in areas with high mountains and forests featuring rugged terrain and poor traffic accessibility, with only a limited number of image characteristic points, the representativeness of error assessment might be adversely influenced due to the lack of sufficient ground measurement points, leading to potential underestimation. There are reported studies in which aerotriangulation or aerial photogrammetry operations were conducted by using high-precision LiDAR DEM data as control points or a reference terrain surface [48–50]. With the six periods of DTM data generated using various techniques in this study, in order to avoid the impacts of insufficient ground control points on error estimation, the DEM data from 2011 were used as the reference elevation. Then the elevation difference between other data sets and the reference at the same image characteristic point could be calculated as $\sigma_{2011\ DEM}$. The error range was 0.43~0.75 m (Table 4), which was higher than σ_{total}. This might be attributed to the fact that in such a densely vegetated area with rugged terrain, the originally measured errors from the ground control points tend to underestimate the elevation. Another possibility was that errors might get magnified when using the 2011 DEM data as reference due to the errors of the reference itself. However, it should be kept in mind that those identifiable spots in bare and flat areas can be selected as characteristic points and only minor errors will be produced when applying ALS in such areas. Moreover, it would be helpful to have a common terrain reference for comparisons between various data sets from different periods. Therefore, it is legitimate to choose at least one period of ALS DEM data as the benchmark for error assessment of multi-period DTM data. Similar concepts could also be applied to forest or mountainous areas with only a few or no control points. For example, after an earthquake or hurricane, when rapid and efficient DTM and orthoimage generation is required or subsequent post-disaster comparisons are needed, one period of ALS data can be used as a terrain reference to select ground control points as needed.

The basic idea of the multi-period DTM error estimation method employed in this paper was to calculate errors using known elevation check points and then to estimate errors between two successive periods using the error propagation equation. The advantage of this approach was that fairly accurate error values could be gained by comparing the known elevation inspection point data with the measured results. However, considering the fact that those identifiable and measurable points are mostly selected in flat, bare, and easily accessible areas, errors might be underestimated due to neglecting the practical slope terrain and vegetation. Moreover, in densely vegetated mountain areas, practical measurable control points are difficult to assign due to the impacts of plants and poor accessibility. An alternative DTM error estimation method is to calculate errors based on the undisturbed terrain areas [25]. The core of this method is to find the elevation differences of the undisturbed area and regard the average value and standard deviation of distribution of elevation difference as the average difference and error range of the two-period DEM, respectively. However, this assessment method tends to be affected by the selected undisturbed areas as the variant areas in mountains/forests might be included in calculations. Hence, one period of ALS data is utilized as the terrain reference for selecting ground control points. In addition to the advantages of the high resolution and precision of the DTM data obtained using ALS, this method can also solve the problem

of insufficiency of elevation check points in areas with high mountains and forests due to measurement difficulties. The work by Podobnikar [51] also proposed the use of a known and high-quality DTM dataset as an important reference for combining different DTM datasets into a better DTM dataset. It applied more rigorous ideas of regionalization and parameter weighting to help improve the quality of the combined DTM data set. In our study, we similarly utilized one period of ALS data as a reference for error estimation but emphasized its convenience and cost-effectiveness for estimating landslide volume under users' demands. As shown in Table 3, the estimated errors of various DTM data sets based on the reference of 2011 DEM do reflect the potential error range of the DEM data.

UAVs have been applied more and more widely in various applications. It has also became one of the common tools for landslide disaster research due to its advantages of low operating cost, high data processing speed, low flying height, convenient flying preparation, and the ease of generating orthoimage and DTM data. Error range evaluation associated with the generated image and DTM data also attracts attention in the research community. The results obtained from this work (Table 3) showed that the error range of DTM data obtained from UAV, which was not equipped with conventional aerial photogrammetry camera, was not significantly different from those of the other three DTM datasets obtained from aircraft equipped with conventional aerial photogrammetry cameras. It should be considered as the optimal choice for investigations over small areas due to its advantages of portability, low cost, and high data processing speed.

Due to the highly unpredictable nature of landslide incidents, few measured landslide volume values exist. It is common practice to evaluate slide volume by measuring the landslide area on the obtained image and then estimating the average depth [26–28]. However, the certainty of landslide depth is often difficult to evaluate due to the lack of terrain information before the disaster, which would affect the accuracy of landslide volume estimation. As a result, there also exist a number of studies where statistical/empirical equations, *i.e.*, relations between area and volume derived by compiling a large quantity of landslide cases, were used to approximate the potential landslide volume based on a certain landslide area. Nevertheless, this type of method is also restricted by various factors such as area features, landslide type, slope morphology, and rock properties [28].

With the utilization of multi-period DTM data in this work, the appearance of the entire landslide area, both before and after, the disaster could be clearly observed thanks to the terrain data obtained from the historical aerial photogrammetry images. The Meiyuan Shan landslide incident with a sliding area of about 0.55 km^2 was analyzed as an example in this paper. In 2008, the disaster produced 16 million m^3 of rock volume, 12 million m^3 of which was deposited in the landslide dam, and 4 million m^3 of which entered the mainstream of Beigang River. The volume changes could be clearly calculated. The use of high-resolution DTM data obtained from multi-period aerial photogrammetry, UAV aerial measurement, and ALS has been proven to be an efficient method to calculate landslide volumes. Specifically, small-area investigations can be implemented using UAV by taking advantage of its portability and speed, whereas large area investigations can employ aerial photogrammetry or ALS to obtain data. Additionally, ALS is also applicable for regional investigations since it possesses the best data precision.

4.2. Profile Comparison

Profiling is a commonly used method in terrain research, among which straight line profiling is the most straightforward, convenient, and rapid approach. As the section AA' shows in Figure 7, the elevation values located on this straight line were selected to generate profiles. Although easy and fast, this approach would also pass non-target areas. Incorporation of unnecessary terrain into the profile would lead to abnormal or irregular terrain information, which might be misleading. Polyline profiling could extract necessary elevation points to generate profiles using a polyline, as the BB' section shows in Figure 8. Compared with the AA' straight line profiling, this approach requires manual selection of polyline sections. Although selection of non-target area data can be mitigated, misleading abnormal, or irregular profiles are still not completely avoidable.

The method of swath profiling has been mostly employed in large-scale terrain applications, such as tectonic structures. However, it was adopted in this work to analyze a small scale slope. Rectangle and the irregular ranges, such as the Meiyuan Shan landslide and the river channel, were used for swath profiling with the minimum amount of horizontal rows. Shown in the top of Figure 8 is a profile based on rectangles, while the irregular shapes of the Meiyuan Shan landslide and the river channel are shown in the bottom of the figure. The major differences between these two were the surroundings of the original landslide on the left and the vicinity of the slope foot, with the rest of the selected elevation values remaining the same. As the profile was based on the minimum values of each row, it could reflect the real landslide situation through the DTM elevation change before and after the disaster, including obvious descent of the original area and clear ascent of the slope middle and the river channel. The trend of elevation change also demonstrated the variations of erosion of the collapse origin and deposition of the rock accumulation area with the profile position. There is a clear elevation change at around 1900 m in the bottom subfigure of Figure 8, which should be the location between the landslide deposition toe and the river channel deposition. This change cannot be observed from the two profiles in Figure 7. Multiple parallel straight line profiling had been previously utilized in landslide discussions [16,52]. Instead, the swath profile method is able to express the landslide terrain using the maxima, minima, or average of each row, which is helpful in landslide interpretation and analysis.

Usually after a landslide event, the sliding sediments would not entirely propagate downstream at once. The remaining body in most cases would be moved downstream due to a subsequent heavy rainfall and, thus, the remaining rocks and the moving earthflow are threats to the downstream area. The ratio between the sediment volume flowing out of the landslide dam and the total sediment volume within the landslide dam can be defined as the sediment delivery rate [21,53,54]. This can represent degrees of erosion and sediment outflow in the water accumulation area and, thereby, provide references for hydraulic engineering or landslide disaster prevention planning. Since we were able to calculate five terrain variations from six DTM data sets, along with the fact that the data we have in this work covered an entire water accumulation area, sediment delivery rate calculations could be conducted. Thus, the sediment volume and the delivery rate of earthflow propagation from this area to the downstream main river channel (Beigang River) could be obtained.

Using the volume around the incident of the Meiyuan Shan landslide as a calculation benchmark, the delivery rates up to 2008, 2011, 2012, and 2013 were 24.6%, 14.3%, 9.8%, and 4.2%, respectively, declining year by year. In fact, the heavy rainfall that occurred during these years also played a critical role. By looking into the total sediment volume generated after the landslide, there were more than six years during which 47.1% of the total volume remained within the landslide dam. This indicated that the sliding sediments would not entirely propagate downstream in a short period of time but, instead, the remaining bulk of these sediments would be moved downstream by subsequent heavy rainfall over time. Therefore, after a landslide, these sediments should be carefully monitored as potential post disaster hazards. Aerial photogrammetry and ALS can be continuously applied after the disaster subsequent to a massive landslide to gather terrain information around the landslide area in order to monitor the terrain changes of the downstream river channel and their potential impacts.

5. Conclusions

For the six periods of DTM data generated in this work, the error of ALS was about 0.15 m–0.18 m, the smallest among these DTM generation techniques. For the four periods of data generated using aerial photogrammetry (including UAV images), the errors of σ_{total} ranged from 0.22 m to 0.40 m. The comparison with the image ground sample distance (GSD) values indicated that σ_{total} error was 0.98–2.1 times that of GSD. This suggested that the precision of the DTM data generated in this work using different aircrafts and generation techniques is suitable for landslide analysis. Especially in mountainous and densely vegetated areas, data generated by ALS can be used as a benchmark to solve the problem of insufficient control points. The error range of DTM data obtained from UAVs was not

significantly different from those of the other three DTM datasets obtained using the traditional aerial photogrammetry technique. This suggested that UAV aerial photogrammetry should be considered as the optimal choice for investigations over small areas due to its advantages of portability, low costs, and speedy data processing.

DTM data were compared in this study to calculate the sediment volume and terrain change before and after the landslide incident. The comparison between the traditional straight line profile and swath profile suggested that the swath profile method is able to express landslide terrain using the maxima, minima, or average of each row, which is helpful in landslide interpretation and analysis. Sediment delivery rate can be determined based on sediment volume change calculated by contrasting DTM data. It was shown that sediment delivery rate decreased each year and was affected by heavy rainfall during each period. Since the Meiyuan Shan landslide in 2007 to 2013, there were more than six years during which approximately half of the total sediment volume remained within the landslide dam. This indicated that the sliding sediments would not entirely propagate downstream in a short period of time. Therefore, after a landslide, these sediments should be carefully monitored as potential post disaster hazards. Aerial photogrammetry and ALS can be applied after the disaster as often as necessary to gather terrain information around the landslide area in order to monitor the terrain changes of the downstream river channel and their potential impacts subsequent to a massive landslide.

Author Contributions: Yu-Chung Hsieh and Yu-Chang Chan developed the scientific concept of the study. Yu-Chung Hsieh carried out data acquisition, analysis and preliminary writing. Yu-Chang Chan coordinated the project together with Jyr-Ching Hu, and contributed to the final writing and revisions of the paper.

Conflicts of Interest: The authors declare no conflicts of interest.

References

1. Oskin, M.E.; Arrowsmith, J.R.; Corona, A.H.; Elliott, A.J.; Fletcher, J.M.; Fielding, E.J.; Gold, P.O.; Garcia, J.J.G.; Hudnut, K.W.; Liu-Zeng, J.; *et al.* Near-Field Deformation from the El Mayor–Cucapah Earthquake Revealed by Differential LIDAR. *Science* **2012**, *335*, 702–705. [CrossRef] [PubMed]

2. Nissen, E.; Krishnan, A.K.; Arrowsmith, J.R.; Saripalli, S. Three-dimensional surface displacements and rotations from differencing pre- and post-earthquake LiDAR point clouds. *Geophys. Res. Lett.* **2012**, *39*. [CrossRef]

3. Glennie, C.L.; Hinojosa-Corona, A.; Nissen, E.; Kusari, A.; Oskin, M.E.; Arrowsmith, J.R.; Borsa, A. Optimization of legacy LiDAR data sets for measuring near-field earthquake displacements. *Geophys. Res. Lett.* **2014**, *41*. [CrossRef]

4. Duffy, B.; Quigley, M.; Barrell, D.J.A.; Van Dissen, R.; Stahl, T.; Leprince, S.; McInnes, C.; Bilderback, E. Fault kinematics and surface deformation across a releasing bend during the 2010 MW 7.1 Darfield, New Zealand, earthquake revealed by differential LiDAR and cadastral surveying. *Geol. Soc. Am. Bull.* **2013**, *125*, 420–431. [CrossRef]

5. Grove, J.R.; Croke, J.; Thompson, C. Quantifying different riverbank erosion processes during an extreme flood event. *Earth Surf. Process. Landf.* **2013**, *38*, 1393–1406. [CrossRef]

6. Heritage, G.; Hetherington, D. Towards a protocol for laser scanning in fluvial geomorphology. *Earth Surf. Process. Landf.* **2007**, *32*, 66–74. [CrossRef]

7. Huang, Y.; Yu, M.; Xu, Q.; Sawada, K.; Moriguchi, S.; Yashima, A.; Liu, C.; Xue, L. InSAR-derived digital elevation models for terrain change analysis of earthquake-triggered flow-like landslides based on ALOS/PALSAR imagery. *Environ. Earth Sci.* **2014**, *73*, 7661–7668. [CrossRef]

8. Tarolli, P. High-resolution topography for understanding Earth surface processes: Opportunities and challenges. *Geomorphology* **2014**, *216*, 295–312. [CrossRef]

9. Ghuffar, S.; Székely, B.; Roncat, A.; Pfeifer, N. Landslide displacement monitoring using 3D range flow on airborne and terrestrial LiDAR data. *Remote Sens.* **2013**, *5*, 2720–2745. [CrossRef]

10. Dewitte, O.; Jasselette, J.C.; Cornet, Y.; Van Den Eeckhaut, M.; Collignon, A.; Poesen, J.; Demoulin, A. Tracking landslide displacements by multi-temporal DTMs: A combined aerial stereophotogrammetric and LiDAR approach in western Belgium. *Eng. Geol.* **2008**, *99*, 11–22. [CrossRef]

11. Peyret, M.; Djamour, Y.; Rizza, M.; Ritz, J.F.; Hurtrez, J.E.; Goudarzi, M.A.; Nankali, H.; Chéry, J.; Le Dortz, K.; Uri, F. Monitoring of the large slow Kahrod landslide in Alborz mountain range (Iran) by GPS and SAR interferometry. *Eng. Geol.* **2008**, *100*, 131–141. [CrossRef]

12. Chen, R.-F.; Chang, K.-J.; Angelier, J.; Chan, Y.-C.; Deffontaines, B.; Lee, C.-T.; Lin, M.-L. Topographical changes revealed by high-resolution airborne LiDAR data: The 1999 Tsaoling landslide induced by the Chi–Chi earthquake. *Eng. Geol.* **2006**, *88*, 160–172. [CrossRef]

13. Chen, Z.; Zhang, B.; Han, Y.; Zuo, Z.; Zhang, X. Modeling accumulated volume of landslides using remote sensing and DTM data. *Remote Sens.* **2014**, *6*, 1514–1537. [CrossRef]

14. Chan, Y.-C.; Chang, K.-J.; Chen, R.-F.; Liu, J.-K. Topographic changes revealed by airborne LiDAR surveys in regions affected by the 2009 Typhoon Morakot, southern Taiwan. *West. Pac. Earth Sci.* **2012**, *12*, 67–82.

15. Corsini, A.; Borgatti, L.; Cervi, F.; Dahne, A.; Ronchetti, F.; Sterzai, P. Estimating mass-wasting processes in active earth slides—Earth flows with time-series of High-Resolution DEMs from photogrammetry and airborne LiDAR. *Nat. Hazards Earth Syst. Sci.* **2009**, *9*, 433–439. [CrossRef]

16. Iverson, R.M.; George, D.L.; Allstadt, K.; Reid, M.E.; Collins, B.D.; Vallance, J.W.; Schilling, S.P.; Godt, J.W.; Cannon, C.M.; Magirl, C.S.; *et al.* Landslide mobility and hazards: Implications of the 2014 Oso disaster. *Earth Planet. Sci. Lett.* **2015**, *412*, 197–208. [CrossRef]

17. Milan, D.J.; Heritage, G.L.; Hetherington, D. Application of a 3D laser scanner in the assessment of erosion and deposition volumes and channel change in a proglacial river. *Earth Surf. Process. Landf.* **2007**, *32*, 1657–1674. [CrossRef]

18. Brasington, J.; Langham, J.; Rumsby, B. Methodological sensitivity of morphometric estimates of coarse fluvial sediment transport. *Geomorphology* **2003**, *53*, 299–316. [CrossRef]

19. Ventura, G.; Vilardo, G.; Terranova, C.; Sessa, E.B. Tracking and evolution of complex active landslides by multi-temporal airborne LiDAR data: The Montaguto landslide (Southern Italy). *Remote Sens. Environ.* **2011**, *115*, 3237–3248. [CrossRef]

20. Lallias-Tacon, S.; Liébault, F.; Piégay, H. Step by step error assessment in braided river sediment budget using airborne LiDAR data. *Geomorphology* **2014**, *214*, 307–323. [CrossRef]

21. DeLong, S.B.; Prentice, C.S.; Hilley, G.E.; Ebert, Y. Multitemporal ALSM change detection, sediment delivery, and process mapping at an active earthflow. *Earth Surf. Process. Landf.* **2012**, *37*, 262–272. [CrossRef]

22. Daehne, A.; Corsini, A. Kinematics of active earthflows revealed by digital image correlation and DEM subtraction techniques applied to multi-temporal LiDAR data. *Earth Surf. Process. Landf.* **2013**, *38*, 640–654. [CrossRef]

23. Bremer, M.; Sass, O. Combining airborne and terrestrial laser scanning for quantifying erosion and deposition by a debris flow event. *Geomorphology* **2012**, *138*, 49–60. [CrossRef]

24. Peng, M.H.; Shih, T.Y. Error assessment in two LiDAR-derived TIN datasets. *Photogramm. Eng. Remote Sens.* **2006**, *72*, 933–947. [CrossRef]

25. Tseng, C.-M.; Lin, C.-W.; Stark, C.P.; Liu, J.-K.; Fei, L.-Y.; Hsieh, Y.-C. Application of a multi-temporal, LiDAR-derived, digital terrain model in a landslide-volume estimation. *Earth Surf. Process. Landf.* **2013**, *38*, 1587–1601. [CrossRef]

26. Guzzetti, F.; Ardizzone, F.; Cardinali, M.; Rossi, M.; Valigi, D. Landslide volumes and landslide mobilization rates in Umbria, central Italy. *Earth Planet. Sci. Lett.* **2009**, *279*, 222–229. [CrossRef]

27. Guzzetti, F.; Ardizzone, F.; Cardinali, M.; Galli, M.; Reichenbach, P.; Rossi, M. Distribution of landslides in the Upper Tiber River basin, central Italy. *Geomorphology* **2008**, *96*, 105–122. [CrossRef]

28. Larsen, I.J.; Montgomery, D.R.; Korup, O. Landslide erosion controlled by hillslope material. *Nat. Geosci.* **2010**, *3*, 247–251. [CrossRef]

29. Central Weather Bureau (CWB); R.O.C. Typhoon Database. Available online: http://rdc28.cwb.gov.tw/ (accessed on 15 December 2015).

30. Water Resources Agency; Ministry of Economic Affairs; R.O.C. Water Resources Agency. Available online: http://eng.wra.gov.tw/ (accessed on 15 December 2015).

31. The Aerial Survey Office; Forestry Bureau; R.O.C. The ASO Historical Aerial Photogrammetry Database. Available online: http://www.afasi.gov.tw/ (accessed on 15 December 2015).

32. Ministry of th Interior; R.O.C. Establishment of The National Coordinate System. Available online: http://gps.moi.gov.tw/SSCenter/Introduce_E/IntroducePage_E.aspx?Page=GPS_E8 (accessed on 15 December 2015).

33. Ministry of th Interior; R.O.C. Taiwan Vertical Datum. Available online: http://gps.moi.gov.tw/SSCenter/Introduce_E/IntroducePage_E.aspx?Page=Height_E4 (accessed on 15 December 2015).

34. Baltsavias, E.P. A comparison between photogrammetry and laser scanning. *ISPRS J. Photogramm. Remote Sens.* **1999**, *54*, 83–94. [CrossRef]

35. Wehr, A.; Lohr, U. Airborne laser scanning—An introduction and overview. *ISPRS J. Photogramm. Remote Sens.* **1999**, *54*, 68–82. [CrossRef]

36. Taylor, J.R. *An Introduction to Error Analysis: The Study of Uncertainties in Physical Measurements*; Univ. Sci. Books: Mill Valley, CA, USA, 1982; p. 327.

37. Prokešová, R.; Kardoš, M.; Medved'ová, A. Landslide dynamics from high-resolution aerial photographs: A case study from the Western Carpathians, Slovakia. *Geomorphology* **2010**, *115*, 90–101. [CrossRef]

38. Müller, J.; Gärtner-Roer, I.; Thee, P.; Ginzler, C. Accuracy assessment of airborne photogrammetrically derived high-resolution digital elevation models in a high mountain environment. *ISPRS J. Photogramm. Remote Sens.* **2014**, *98*, 58–69. [CrossRef]

39. Hodgson, M.E.; Bresnahan, P. Accuracy of airborne LiDAR-derived elevation: Empirical assessment and error budget. *Photogramm. Eng. Remote Sens.* **2004**, *70*, 331–339. [CrossRef]

40. Orem, C.A.; Pelletier, J.D. Quantifying the time scale of elevated geomorphic response following wildfires using multi-temporal LiDAR data: An example from the Las Conchas fire, Jemez Mountains, New Mexico. *Geomorphology* **2015**, *232*, 224–238. [CrossRef]

41. Benjamin, M.J.; Jason, M.S.; Ann, E.G.; Guido, G.; Vladimir, E.R.; Thomas, A.D.; Nicole, E.M.K.; Bruce, M.R. Quantifying landscape change in an arctic coastal lowland using repeat airborne LiDAR. *Environ. Res. Lett.* **2013**, *8*, 925–932.

42. Rumsby, B.; Brasington, J.; Langham, J.; McLelland, S.; Middleton, R.; Rollinson, G. Monitoring and modelling particle and reach-scale morphological change in gravel-bed rivers: Applications and challenges. *Geomorphology* **2008**, *93*, 40–54. [CrossRef]

43. Telbisz, T.; Kovács, G.; Székely, B.; Szabó, J. Topographic swath profile analysis: A generalization and sensitivity evaluation of a digital terrain analysis tool. *Z. Geomorphol.* **2013**, *57*, 485–513. [CrossRef]

44. Burbank, D.W.; Blythe, A.E.; Putkonen, J.; Pratt-Sitaula, B.; Gabet, E.; Oskin, M.; Barros, A.; Ojha, T.P. Decoupling of erosion and precipitation in the Himalayas. *Nature* **2003**, *426*, 652–655. [CrossRef] [PubMed]

45. Clarke, B.A.; Burbank, D.W. Bedrock fracturing, threshold hillslopes, and limits to the magnitude of bedrock landslides. *Earth Planet. Sci. Lett.* **2010**, *297*, 577–586. [CrossRef]

46. Robl, J.; Hergarten, S.; Stüwe, K. Morphological analysis of the drainage system in the Eastern Alps. *Tectonophysics* **2008**, *460*, 263–277. [CrossRef]

47. Reutebuch, S.E.; McGaughey, R.J.; Andersen, H.-E.; Carson, W.W. Accuracy of a high-resolution LiDAR terrain model under a conifer forest canopy. *Can. J. Remote Sens.* **2003**, *29*, 527–535. [CrossRef]

48. Liu, X.; Zhang, Z.; Peterson, J.; Chandra, S. LiDAR-derived high quality ground control information and DEM for image orthorectification. *GeoInformatica* **2007**, *11*, 37–53. [CrossRef]

49. Gneeniss, A.S.; Mills, J.P.; Miller, P.E. In-flight photogrammetric camera calibration and validation via complementary LiDAR. *ISPRS J. Photogramm. Remote Sens.* **2015**, *100*, 3–13. [CrossRef]

50. Gneeniss, A.S.; Mills, J.P.; Miller, P.E. Reference LiDAR surfaces for enhanced aerial triangulation and camera calibration. *Int. Arch. Photogramm. Remote Sens. Spat. Inf. Sci.* **2013**, *1*, 111–116. [CrossRef]

51. Podobnikar, T. Production of integrated digital terrain model from multiple datasets of different quality. *Int. J. Geogr. Inf. Sci.* **2005**, *19*, 69–89. [CrossRef]

52. Kasperski, J.; Delacourt, C.; Allemand, P.; Potherat, P.; Jaud, M.; Varrel, E. Application of a terrestrial laser scanner (TLS) to the study of the Séchilienne Landslide (Isère, France). *Remote Sens.* **2010**, *2*, 2785–2820. [CrossRef]

53. Tseng, C.-M.; Lin, C.-W.; Chang, K.-J. The Sediment Budgets Evaluation in a Basin Using LiDAR DTMs. In *Engineering Geology for Society and Territory*; Springer: Berlin, Germany; Heidelberg, Germany, 2015; Volume 3, pp. 37–41.

54. Mackey, B.H.; Roering, J.J. Sediment yield, spatial characteristics, and the long-term evolution of active earthflows determined from airborne LiDAR and historical aerial photographs, Eel River, California. *Geol. Soc. Am. Bull.* **2011**, *123*, 1560–1576. [CrossRef]